Wear behavior at high temperatures of ZrO2 - Al2O3 plasma sprayed coatings and an electro-melted AZS refractory

D. Franco, H. Ageorges, E. López, F. Vargas

Version of Record: https://www.sciencedirect.com/science/article/pii/S0257897221008896
Manuscript_3c6d8196617e01e75857110590f1e362

WEAR BEHAVIOR AT HIGH TEMPERATURES OF ZrO_2 - Al_2O_3 PLASMA SPRAYED COATINGS AND AN ELECTRO-MELTED AZS REFRACTORY

D. Franco [a, b, c, *], H. Ageorges [a], E. López [b] and F. Vargas [b]

[a] Université de Limoges (Limoges – France), ECNRS, IRCER, UMR7315, F-87000.

[b] Universidad de Antioquia (Medellín – Colombia), GIPIMME-GIMACYR Research Groups.

[c] Tecnológico de Antioquia (Medellín – Colombia), CBATA Research Group.

[*] Corresponding author: idavid.franco@udea.edu.co

Abstract

Two ZrO_2-Al_2O_3 atmospheric plasma coatings were applied to a pressed and sintered aluminosilicate refractory brick, which were compared to an electro-melted alumina-zirconia-silica (AZS) refractory typically used in the glass industry for its high temperature wear resistance. The samples were subjected to sliding contact using a ball-on-disk test at 25, 500, 750, and 1000 °C and then, physical, crystallographic, and mechanical characterizations were performed before and after the wear tests in order to monitor the wear behaviour. Both ZrO_2-Al_2O_3 coatings exhibited better wear performance than the electro-melted AZS refractory at all temperatures evaluated, owing to their high hardness and fracture toughness, which were mainly related to the increase of α-Al_2O_3 and t-ZrO_2 phases from γ-Al_2O_3 and the crystallization of amorphous phases respectively. In the same way, both coatings also showed the same wear mechanisms at all temperatures evaluated. At 25 °C, wear by ductile deformation was identified, while at 500 and 750 °C, wear by brittle deformation was produced, and at 1000 °C, the transition of wear from brittle to ductile deformation was evident. For the electro-melted AZS refractory, until 750 °C, wear by brittle deformation was developed, while at 1000 °C, wear by both, brittle and ductile deformation was detected.

Keywords

ZrO_2-Al_2O_3 coatings, AZS refractory, high temperature, tribological behavior.

1. NTRODUCTION

Electro-melted alumina-zirconia-silica (AZS) refractories are widely used in glass melting furnaces [1-4] because of their thermal shock resistance and resistance to both corrosive and tribological wear when they are subjected to molten glass [1]. However, these refractories are the most expensive components within the glass industry. Therefore, reducing the costs associated with installation, operation, and maintenance of these refractories is critical for the glass industry to compete with plastic, aluminum, and other types of packaging.

Alumina is used in AZS refractories because of its high hardness and good corrosion resistance, despite its relatively low fracture toughness compared to zirconia. In contrast, zirconia exhibits high strength and good fracture toughness, but has low hardness [1, 5]. The tetragonal to monoclinic phase transformation produced above 1000 °C in ZrO_2 causes a significant change in volume (3% – 5%), which can lead to cracking during cooling of this material. However, in AZS refractories, this volume change can be dissipated by the presence of a glassy phase promoted by the silica contained in these materials, which constitutes approximately 30% of their volume [1].

Plasma sprayed zirconia-alumina coatings used as thermal barriers have been studied by other authors for their mechanical properties and oxidation resistance [6-7]. These coatings demonstrate good mechanical and chemical properties, as well as good oxidation resistance without compromising their thermal behavior. Furthermore, the combination of the high hardness of alumina with the low thermal conductivity of zirconia contributes to the development of both the thermal shock and wear resistance of these coatings [7]. In addition to the crystalline phases of alumina and zirconia, amorphous phases are also present [8-10],

which could play an important role in the tribological performance of the coatings when heated above the crystallization temperature (920 °C) [8].

In this study, the tribological behavior of three ZrO_2-Al_2O_3 based materials at different temperatures was analyzed. Two ZrO_2-Al_2O_3 coatings were thermally sprayed on a pressed and sintered aluminosilicate brick, and the properties were compared to an electro-melted AZS refractory. To the best of our knowledge, previous studies have not reported on these materials and conditions. Furthermore, the results suggest that ZrO_2-Al_2O_3 coatings could be applied to protect conventionally pressed and sintered refractories subjected to extreme abrasive conditions, thereby replacing expensive electro-melted refractories for non-structural applications.

2. MATERIALS AND METHODS

To manufacture the ceramic coatings, either a ZrO_2-Al_2O_3 Eutectic–Castolin 25088™ (agglomerated and sintered) or a ZrO_2-Al_2O_3-Y_2O_3 Tosoh TZ-3Y20A™ (mixed and crushed) feedstock powder was thermally sprayed on a substrate using a Sulzer-Metco PTF4™ plasma torch according to the parameters listed in Table 1. The substrate was a conventionally pressed and sintered aluminosilicate refractory brick ER-40™ manufactured by ERECOS S.A., which was cut into short samples (25 mm in diameter and 7 mm in height). Additionally, an electro-melted alumina-zirconia-silica (AZS) refractory Monofrax CS5™ was used as the reference sample.

The chemical and crystallographic characterization of the feedstock powders was carried out by wavelength-dispersive X-ray fluorescence (WD-XRF) and X-ray diffraction (XRD) using

a Thermo Fisher SCIENTIFIC ARL™ OPTIM'X spectrometer and a Bruker D8 ADVANCE X-Ray Cu Kα 1 radiation (XRD) diffractometer, respectively. Additionally, the Rietveld method was used to quantify the phases identified by XRD using the following COD cards: 1) α-Al_2O_3 (9009674), 2) γ-Al_2O_3 (1010461), 3) t-ZrO_2 (1525706), 4) m-ZrO_2 (1010912) and 5) Mullite (9001567). Furthermore, the particle size distribution was determined by laser diffraction (LD) with a Horiba PARTICA LA-950V2, and their morphological characterization was performed by scanning electron microscopy (SEM) using a JEOL JSM IT-300 LV microscope.

The cross-section and surface of the three samples (the two coatings and the AZS refractory used as a reference) were ground and polished according to the ASTM E1920 standard [11] with the aim of obtaining an arithmetic average roughness (Ra) lower than 0.2 µm to evaluate their structure, mechanical properties, and tribological performance. The structures of both the coatings and the electro-melted refractory were evaluated by SEM using the previously mentioned microscope. This evaluation was carried out on both the as-sprayed surface and the polished cross section of the coatings, while only the surface of the electro-melted refractory was analyzed owing to the isotropic characteristics of its structure. The porosity in the structure was measured from images taken at 200× by SEM using the backscatter electron beam following the procedure outlined in the ASTM E2109 standard [12] and using Image J software.

The crystallographic phases of all samples were determined by XRD complemented with Rietveld analysis using the same diffractometer, while the mechanical properties were determined from indentations performed on the polished surface using a Shimadzu HMV-G 20 according to ASTM C-1327 [13]. The microhardness and fracture toughness were calculated from residual indents and cracks produced by Vickers indentation, while the

Young's modulus was calculated from the Knoop indentation. It is important to note that in the ASTM C-1327 standard established for Vickers hardness, at least 10 acceptable indentations meeting an acceptance criterion must be obtained by applying a force for 15 s (3 N for the samples evaluated in this study) that does not change the hardness of the material with the applied load. The fracture toughness was calculated from the length of the radial/median cracks (according to C >2a criterion, where C is the crack length and a is the average of the indent diagonals, measured from the center of the Vickers indent produced by applying a load of 10 N for 15 s as it is shown in Figure 1 a. For the Young's modulus, a load of 3 N was applied to the Knoop indenter as it is shown in Figure 1 b. The micro-hardness, Young's modulus, and fracture toughness were calculated according to Eqs. (1)–(3), respectively:

$$H_V = 0.0018544 \frac{P_N}{d^2} \qquad \text{Eq. (1)}$$

Where H_V is the Vickers micro-hardness [GPa], P_N is the applied normal load on the indenter [N], and d is the average length of the two diagonals produced during the indentation [mm].

$$E = \frac{-\alpha H_K}{\left(\frac{b'}{a'} - \frac{b}{a}\right)} \qquad \text{Eq. (2)}$$

Where E is the Young's modulus [GPa], α is a constant ($\alpha = 0.45$), H_k is the Knoop microhardness [Pa], $a'$and $b'$are the longer and shorter diagonals, respectively, produced by the indentation [µm], and a and b are the geometric constants of the indenter ($b/a = 1/7.11$).

$$K_{IC} = 0.0016\sqrt{\frac{E}{H_v}}\frac{P_N}{C^{3/2}} \quad \text{Eq. (3)}$$

Where K_{IC} is the fracture toughness [MPa.m$^{1/2}$], E is the Young's modulus [GPa], H_v is the Vickers micro-hardness [GPa], P_N is the applied normal load on the indenter [N], and C is the longest radial crack produced during the indentation [mm] [14].

On the other hand, the wear tests of all samples were carried out using a homemade ball-on-disk tribometer under dry sliding contact at temperatures of 25, 500, 750, and 1000 °C, using an alumina ball 6 mm in diameter as counter-body, applying a load of 5 N during 20000 cycles and rotating the samples at a linear speed of 0.1 ms^{-1} without eliminating the formed debris, according to the recommendations of the ASTM G-99 standard [15] shown in Table 2.

The wear tracks were analyzed by SEM using the aforementioned microscope as well as by optical microscopy (OM) using an Olympus BX41 microscope. To calculate the wear rate produced for each sample, Eq. (4) was used. The average cross-sectional area (A_s) for each wear track was determined from the analysis of profiles at 10 different points using a Surtronic S125 profilometer as it is shown in Figure 2.

$$WR_{Sample} = \frac{Volume}{Load \times Distance} = \frac{A_s 2\pi r_{wt}}{1000 P_N N_c 2\pi r_{wt}} \quad \text{Eq. (4)}$$

Where WR_{Sample} is the wear rate [mm^3/N.m], A_s is the wear track cross-sectional area [µm^2], r_{wt} is the wear track radius [mm], P_N is the applied normal load [N], and N_c is the total cycle number. In the same way, to calculate the wear rate produced for each counter-body, Eq. (5) was used. The height (h) for each worn counter-body was determined from 10 different measurements using an electronic Rexbeti micrometer.

$$WR_{Counter-body} = \frac{Volume}{Load \times Distance} = \frac{\frac{1}{3}\pi h^2(3R-h)}{P_N D_T} \quad \text{Eq. (5)}$$

where $WR_{Counter-body}$ is the wear rate [mm^3/N.m], h is the height of the spheric cap [mm], R is the counter-body diameter [mm], P_N is the applied normal load [N], and D_T is the total distance of the tests [m].

After the tribological tests, the porosity, crystallographic phases, micro-hardness, Young's modulus, and fracture toughness of all samples were evaluated as described above, in order to determine possible changes produced during the wear tests performed at different temperatures. Each property was determined before and after the wear tests using three samples, and the mechanical properties were tested 10 times for each sample, guaranteeing statistical reproducibility and repeatability for all measurements.

3. RESULTS

3.1. Characterization of feedstock powders

The results of the chemical composition, phases, and particle size distribution of the feedstock powders used to manufacture the bimodal and monomodal coatings are summarized in Table 3. Both powders consisted mainly of ZrO_2 and Al_2O_3, with low quantities of Y_2O_3, Na_2O, and MgO. Consequently, m-ZrO_2 and α-Al_2O_3 were identified as crystalline phases. The particle size distribution of the Eutectic–Castolin 25088^{TM} powder was d_{10}=15.25 µm and d_{90}=94.12 µm, while that for Tosoh TZ-3Y20A^{TM} was d_{10}=29.82 µm and d_{90}= 57.12 µm. Morphological analysis indicated that the Eutectic–Castolin 25088^{TM} powder corresponded to rounded granules composed of micron-sized particles, which are characteristic of those manufactured

by agglomeration and sintering processes (Figure 3 a). For the Tosoh TZ-3Y20A™ powder, sharp particles and fracture patterns were identified, which is characteristic of feedstock processed by crushing (Figure 3 b).

3.2. Structural characterization of samples

Structural analysis of both the as-sprayed surface and the polished cross section of the Eutectic–Castolin 25088™ coating powder was characterized by partially melted particles (Figures 4 a-b) embedded in the splats and lamellae, respectively. The partially melted particles embedded in the molten material produced a bimodal coating on the structure of the substrate. In contrast, the structure of the coating sprayed from the Tosoh TZ-3Y20A™ powder exhibited only splats, lamellae, and pores, which are characteristics of thermally sprayed coatings with a monomodal structure (Figures 4 c-d). The thickness of the bimodal coating manufactured from the Eutectic–Castolin 25088™ powder was 215±20 µm, while that of the monomodal coating sprayed from the Tosoh TZ-3Y20A™ was 260±25 µm. The porosity value measured on the cross sections of both samples was higher in the bimodal coating (8.0 ±1.0%) than in the monomodal coating (7.1±1.1%) due to the presence of partially melted particles that hindered the stacking of sprayed particles. The structural analysis of the electro-melted AZS refractory revealed zirconia–alumina dendrites in an amorphous matrix phase that was highly densified (Figure 4 e), resulting in a very low porosity (0.30 ± 0.05 %). Specifically, the white particles in the dendrites shown in Figure 4 e correspond to the tetragonal zirconia phase, while the light gray particles are alpha alumina, and the dark gray region is the amorphous phase. The porosities measured before and after the tribological tests are shown in Figure 5, and the results indicate that the temperatures of the wear tests for all three samples did not promote sintering.

3.3. Crystallographic characterization of samples

The phase analysis established that both coatings consisted mainly of an amorphous phase (> 50 wt.%) with α-Al_2O_3 and γ-Al_2O_3 phases and smaller quantities of t-ZrO_2 and m-ZrO_2 phases (Figures 6 a-b). The γ-Al_2O_3 phase in these coatings was produced from the α-Al_2O_3 phase transformation produced during the thermal spraying process, as previously described [16-22]. These results are in agreement with those of other authors who have reported the presence of large quantities of amorphous phases [23], as well as α-Al_2O_3, γ-Al_2O_3, t-ZrO_2, and m-ZrO_2 phases, in plasma-sprayed coatings from feedstock powders with different proportions of Al_2O_3 and ZrO_2 [23-24]. In comparison, the electro-melted AZS refractory phase analysis indicated that it consisted mainly of amorphous phases (~42 wt.%), t-ZrO_2 (~28 wt.%), α-Al_2O_3 (~22 wt.%), and mullite (~7 wt.%) (Figure 6 c), corresponding to the crystallographic compositions previously reported [25].

Figures 7 a-c show that some phases present in our samples had significant changes after heating to 1000 °C during the tribological tests. In both coatings, the t-ZrO_2 phase increased significantly at the expense of the amorphous phase, as previously reported by other authors [23]. For the electro-melted AZS refractory, a small increase in both phases, t-ZrO_2 and α-Al_2O_3, was produced by crystallization of its amorphous phase. These results indicate that in both coatings, the amorphous phase corresponded to low-crystallinity t-ZrO_2, while the electro-melted AZS refractory consisted of a glassy phase related to the approximately 30 vol% SiO_2 in its composition.

3.4. Mechanical characterization of samples

The results of the mechanical characterization performed before and after the tribological tests are presented in Figures 8 a-c. In general, it is possible to see a slight increase in the hardness

of both coatings after exposure to 1000 °C during the tribological tests, which can be correlated to the changes in the crystalline phases (Figures 6-7 a-c). The Young's modulus for all samples did not indicate significant differences after exposure to different temperatures during the wear tests, which indicates that this mechanical property is not very sensitive to the crystallization of amorphous phases produced at 1000 °C. The fracture toughness did not change for the bimodal coating at any temperature, even at 1000 °C, however, for the monomodal coating, these values were stable until 750°C and decreased at 1000 °C. For the electro-melted AZS refractory, the mechanical properties did not change significantly as a function of temperature, mainly because of the low values of crystallization from the amorphous phase to the t-ZrO_2 and α-Al_2O_3 phases, as well as the minimal changes in porosity.

3.5. Wear characterization of samples

The wear rate results of the ZrO_2-Al_2O_3 coatings and the electro-melted AZS refractory are presented in Figure 9, where it is possible to see that for all materials evaluated, the highest wear rates were obtained at 500 and 750 °C, while the lowest ones were obtained at 25 and 1000 °C, which is related to the crystallographic phases and therefore to the mechanical properties of these materials.

The analysis of wear tracks produced in the three samples showed the development of different tribological mechanisms depending on the test temperature. For both ZrO_2-Al_2O_3 coatings tested at 25 °C, regular wear tracks, with plastic deformation and without any sign of fracture where observed (Figures 10-11 a-c). Meanwhile, at 500 and 750 °C, irregular wear tracks, with sings of microcracks and detachment of particles were evident (Figures 10-11 d-i). Furthermore, at 1000 °C, again regular wear tracks were identified, but this time with continuous layers composed of fine debris, in which plastic flow was observed (Figures 10-11

j-l). In contrast, a regular wear track, with evidence of plastic deformation and cracking mainly produced in the amorphous phase were observed in the wear track of the electro-melted AZS refractory tested at 25 °C (Figures 12 a-c). At 500 °C, in addition to the plastic deformation of the amorphous phase, the detachment of both zirconia and the surrounding amorphous phase was also observed, producing irregular wear tracks (Figures 12 d-f). Additionally, in samples tested at 750 °C, the detachment of both zirconia dendrites and the surrounding amorphous phase was accentuated, producing wear tracks also irregular (Figure 12 g-i). These detachments were even more pronounced in samples evaluated at 1000 °C, despite the discontinuous layer formed from debris (Figure 12 j-l).

The friction coefficient values (Figure 13) measured during the tribological tests did not indicate a particular trend with respect to the temperature. However, in general, they were lower for the samples evaluated at 1000 °C, likely due to the reduction in the severity of the tribological contact by the layer formed from debris. The coefficient of friction values were similar to those previously reported for ZrO_2-based materials against alumina [26].

Figure 14 showed that the counter-body wear rates increased with the temperature until 750°C, and then at 1000°C, these rates decreased, which was probably related to the aforementioned changing in crystallographic phases and mechanical properties, and therefore in the tribological mechanisms. Additionally, from Figures 15, it is clear that on the worn surfaces of the counter-bodies, there were signs of friction traces as expected for abrasive wear, and there is not any sign of wear by adhesion.

4. DISCUSSION

In general, the hardness of all samples is governed by the phases that constitute them. In this case, both ZrO_2-Al_2O_3 based coatings containing ~40 wt.% of alumina phases (α-Al_2O_3 and γ-Al_2O_3) had a higher hardness than the AZS electro-melted refractory whose alumina phase content was ~22 wt.%. Alumina phases are harder than the zirconia and mullite phases present in these three specimens [27-30]. Additionally, the increase in the α-Al_2O_3 phase at the expense of the γ-Al_2O_3 phase when the spray coated samples were heated to 1000 °C was evident and it is widely reported [16-22], while the increase in the α-Al_2O_3 phase detected after heating the electro-melted AZS refractory at 1000 °C was due to crystallization of the amorphous phase. Previous studies have demonstrated crystallization of the amorphous phase in Al_2O_3-ZrO_2 materials from temperatures close to 950 °C [23]. In the same way, the hardness also increased because of the increase in the t-ZrO_2 phase produced by the crystallization of the amorphous phase during the wear tests at 1000 °C. The t-ZrO_2 crystals have higher hardness values (~16 GPa) [31] than those of the ZrO_2 amorphous phase (~12.0 GPa) [31].

Concerning the crack propagation resistance, the AZS electro-melted refractory displayed a lower fracture toughness than both coatings because its amorphous phase corresponded mainly to a glassy phase, whereas the high volume of amorphous phase in the coatings was a low-crystallinity t-ZrO_2. The high propagation of cracks in vitreous materials has been previously reported by other authors [32]. Additionally, the fracture toughness values after the tests at 1000 °C decreased significantly for the monomodal coating, whereas it did not change for the bimodal coating. The fracture toughness of the bimodal coating samples after the high

temperature tribological tests did not decrease because of the presence of partially melted particles that may have contributed to the arrest of the cracks.

The microcracks produced during the sliding of the counter-body on the three samples were due to fatigue fracture, as has been previously reported by other authors for ZrO_2-based materials [33-35]. Fatigue fracture and particle detachment are characteristics of a special kind of abrasive wear mechanism applied only to ceramics called wear by brittle deformation, which is produced when the stresses applied by sliding contact with a hard counter-body are higher than the mechanical resistance of the samples [36]. Additionally, other authors have indicated that the wear resistance of ceramic materials depends on both their hardness and fracture toughness [37-39]. In this case, the Vickers microhardness and fracture toughness of both ZrO_2-Al_2O_3 coatings before and after tribological testing were higher than those of the electro-melted AZS refractory, which makes the latter sample more prone to wear by brittle deformation. Additionally, the adhesion of debris to the wear track surface promotes the formation of layers, as evidenced by samples tested at 1000 °C. The layers modify the conditions of sliding contact, reduce cracks and detachment of particles, and therefore produce a plastic deformation typical of a special kind of abrasive wear mechanism applied only to ceramics called wear by ductile deformation [33, 36, 40]. The microcracks and detachment of particles were more accentuated by increasing temperature when the wear was produced by brittle deformation.

When wear was governed by ductile deformation in samples tested at 25 °C, the wear rates were lower than those tested at 500 and 750 °C, which were controlled by brittle deformation. The increase in wear rate with increasing temperature is because the hardness of the alumina, zirconia, and glass (as the amorphous phase in the electro-melted AZS refractory) decreases with increasing temperature [41-42], followed by a possible softening of the samples as the

temperature of each tribological test increased. This softening may have also affected the alpha alumina ball used as a counter-body, but in a lower proportion owing to its lower porosity (lower than 0.1) than that of the samples. The decrease in the hardness of the samples made them more prone to wear by brittle deformation, increasing the cracking and detachment of particles from the wear track with increasing temperature. However, when the samples were subjected to 1000 °C, some changes in their phases and, perhaps, a partial recovery of their mechanical properties was produced. In both coatings, the amorphous phase crystallized to the t-ZrO_2 phase and γ-Al_2O_3 transformed to the α-Al_2O_3 phase, which increased the content of these phases in the coatings by ~25 wt.% and ~4 wt.%, respectively. On the other hand, in the electro-melted AZS refractory, the crystallization of the amorphous phase to both t-ZrO_2 and α-Al_2O_3 phases was evident, which increased the content of these phases in the sample to ~4 wt.% and ~2 wt.%. These phase transformations may have increased the hardness of the samples, since t-ZrO_2 is harder than the amorphous phase from which it was produced [31] and α-Al_2O_3 is harder than γ-Al_2O_3 [16, 43-44].

The increase in the harder phases in the samples tested at 1000 °C may have helped to counteract the progressive softening produced with increasing temperature, and also may have contributed to the change in the tribological mechanism from wear by brittle deformation to wear by ductile deformation, mainly in the coatings. Additionally, the layer on the 1000 °C samples with apparent plastic flow on the wear tracks indicated that the softening of samples produced the formation of this layer, reducing the severity of the tribological contact. This led to a decrease in the wear rate of the samples evaluated at 1000 °C compared to those tested at 500 and 750 °C.

It is important to note that the wear rate produced at all temperatures was lower for the coatings than for the electro-melted AZS refractory. This is due to the higher hardness and

fracture toughness of the coatings (Figure 8 a), in agreement with other authors who find that the wear resistance of ceramic materials increases with these mechanical properties [37-39]. Additionally, the wear rate produced in the bimodal coating was lower than that in the monomodal coating, suggesting that the presence of partially melted particles, which may have retained some of the agglomerated fine particles in the structure of this coating, can improve its wear resistance.

5. CONCLUSIONS

The tribological behavior at different temperatures of bimodal and monomodal plasma-sprayed ZrO_2-Al_2O_3 coatings were evaluated and compared to an electro-melted AZS refractory. The wear behavior of these materials correlated to their mechanical properties, which is a function of their crystalline phases. The mechanical properties and crystalline phases were measured before and after the tribological tests. The changes in the wear mechanism as a function of the temperature were identified.

The wear mechanisms identified in both plasma-sprayed ZrO_2-Al_2O_3 coatings were as follows: ductile deformation at 25 °C, brittle deformation at 500 and 750 °C, and ductile deformation at 1000 °C. In contrast, wear by both brittle and ductile deformation was identified at 25 °C for the electro-melted AZS refractory, while wear by brittle deformation was identified at 500 and 750 °C. At 1000 °C, wear owing to both brittle and ductile deformation was identified again. These behaviors were related to possible changes in their mechanical properties owing to the softening produced in the alumina, zirconia, and glass (as the amorphous phase in the electro-melted AZS

refractory) with the increase in temperature, as well as the partial recovery of the hardness by crystallization of harder phases at 1000 °C.

- The ZrO_2-Al_2O_3 coatings produced a higher wear resistance at all evaluated temperatures than the electro-melted AZS refractory, mainly because of their higher hardness and fracture toughness. The hardness of the coatings was higher than that of the AZS refractory, mainly owing to the high content of alumina phases. On the other hand, the fracture toughness of the electro-melted AZS refractory was lower than that of the coatings because the amorphous phase corresponded mainly to a brittle glassy phase, whereas the amorphous phase in the coatings was a low-crystallinity t-ZrO_2.

- The low-cost pressed and sintered refractories coated with a zirconia-alumina plasma sprayed layer could replace the expensive electro-melted AZS refractories for abrasive and non-structural applications, such as combustion ports and batch houses, in the glass and cement industries.

6. ACKNOWLEDGEMENTS

- The authors are grateful to Departamento Administrativo de Ciencia, Tecnologia e Innovacion – Colciencias – (Bogotá – Colombia). Convocatoria Doctorado Nacional – 647 de 2014 for the Doctoral Fellowship awarded to David Franco and the CODI-Committee of the University of Antioquia for its economic support given to both the GIPIMME – GIMMACYR research groups in 2019 and the FIT 1-1-01 project.

7. REFERENCES

1. G. I. Vázquez, J. L. Rodríguez, J. C. Rendón, J. López, C. A. Gutiérrez, Microstructure and mechanical behavior of alumina – zirconia – mullite refractory materials, Ceramics International 38 (2012) 1617 – 1625
2. V. Y. Dzyuzer, Electrofused AZS Refractories for High – Capacity Glass – Founding Furnaces, Refractories and Industrial Ceramics 54 (2013) 304 – 306
3. V. Y. Dzyuzer, Features of Initial Heating of Glass – Founding Furnaces, Refractories and Industrial Ceramics 56 (2015) 17 – 19
4. A. M. Guzmán, D. I. Martínez, R. González, Corrosion – erosion wear of refractory bricks in glass furnaces, Engineering Failure Analysis 46 (2014)188 – 195
5. D. Sarkar, S. Adak, M. C. Chu, S. J. Cho, N. K. Mitra, Influence of ZrO_2 on the thermo-mechanical response of nano-ZTA, Ceramics International Volume 33, Issue 2, March 2007, Pages 255-261
6. S. Widjaja, A. M. Limarga, T. H. Yip, Oxidation behavior of a plasma – sprayed functionally graded ZrO_2/Al_2O_3 thermal barrier coating, Materials Letters 57 [3] (2002) 628 – 634
7. B. Liang, H. Liao, C. Ding, C. Coddet, Nanostructured zirconia – 30 vol.% alumina composite coatings deposited by atmospheric plasma spraying, Thin Solid Films 484 [1–2] (2005) 225 – 231
8. X. Song, T. Suhonen, T. Varis, L. Huang, X. Zheng, Y. Zeng, Fabrication and Characterization of Amorphous Alumina – Yttria – Stabilized Zirconia Coatings by Air Plasma Spraying, Journal of Thermal Spray Technology 23 (2014) 1302 – 1311
9. F. Tarasi, M. Medraj, A. Dolatabadi, J. Oberste – Berghaus, C. Moreau, Structural considerations in plasma spraying of the alumina – zirconia composite, Surface and Coatings Technology 205 [23–24] (2011) 5437 – 5443

10. Y. Chen, Y. Yang, Z. Chu, X. Chen, L. Wang, Z. Liu, Y. Dong, D. Yan, J. Zhang, Z. Kang, Microstructure and properties of Al_2O_3-ZrO_2 composite coatings prepared by air plasma spraying, Applied Surface Science 431 (2018) 93 – 100
11. ASTM E – 1920, Standard guide for metallographic preparation of thermal sprayed coatings, reapproved 2014
12. ASTM E – 2109, Standard test methods for determining area percentage porosity in thermal sprayed coatings, reapproved 2014
13. ASTM C – 1327, Standard test method for Vickers indentation hardness of advanced ceramics, 2015
14. G. R. Anstis, P. Chantikul, B. R. Lawn, D. B. Marshall, A Critical Evaluation of Indentation Techniques for Measuring Fracture Toughness: I, Direct Crack Measurement, Journal of the American Ceramic Society 64 [9] (1981) 533 – 538
15. ASTM G – 99, Standard test method for wear testing with a pin – on – disk apparatus, 2017
16. J. W. Murray, A. S. M. Ang, Z. Pala, E. C. Shaw, T. Hussain, Suspension High Velocity Oxy – Fuel (SHVOF) – Sprayed Alumina Coatings: Microstructure, Nanoindentation and Wear, Journal of Thermal Spray Technology 25 [8] (2016) 1700 – 1710
17. G. N. Heintze, S. Uematsu, Preparation and structures of plasma – sprayed γ– and α– Al_2O_3 coatings, Surface & Coatings Technology 50 (1992) 213 – 222
18. K. Sabiruddin, J. Joardar, P.P. Bandyopadhyay, Analysis of phase transformation in plasma sprayed alumina coatings using Rietveld refinement, Surface & Coatings Technology 204 (2010) 3248 – 3253
19. G. Di Girolamo, A. Brentari, C. Blasi, E. Serra, Microstructure and mechanical properties of plasma sprayed alumina – based coatings, Ceramics International 40 (2014) 12861 – 12867

20. R. McPherson, A review of microstructure and properties of plasma sprayed ceramic coatings, Surface & Coatings Technology 39/40 (1989) 173 – 181
21. R. McPherson, On the formation of thermally sprayed alumina coatings, Journal of Materials Science 15 (1980) 3141 – 3149
22. P. Chráska, J. Dubsky, K. Neufuss, J. Pisacka, Alumina – base plasma – sprayed materials. Part I: Phase stability of alumina and alumina – chromia, Journal of Thermal Spray Technology 6 [3] (1997) 320 – 326
23. H. J. Kim, Y. J. Kim, Amorphous phase formation of the pseudo-binary Al_2O_3 – ZrO_2 alloy during plasma spray processing, Journal of Materials Science 34 (1999) 29 – 33
24. A. González, H. Ageorges, O. Rojas, E. López, F. Hurtado, F. Vargas, Efecto de la microestructura y de la microdureza sobre la resistencia al desgaste de recubrimientos elaborados por proyección térmica por plasma atmosférico a partir de circona – alúmina, circona – itria y circona – ceria, Boletín de la Sociedad Española de Cerámica y Vidrio 54 (2015) 124 – 132
25. M. S. Conconi, N.M. Rendtorff, E.F. Aglietti, Evaluation of non-crystalline phase in AZS refractories by XRD Methods, New Journal of Glass and Ceramics 1 (2011) 28 – 33
26. C. S. Yust, F. J. Carignan, Observations on the sliding wear of ceramics, ASLE Transactions 28 (1985) 245 – 253
27. K. A. Habib, J.J. Saura, C. Ferrer, M. S. Damra, E. Giménez, and L. Cabedo, Comparison of flame sprayed Al_2O_3/TiO_2 coatings: Their microstructure, mechanical properties and tribology behavior, Surface & Coatings Technology 201 (2006) 1436 – 1443
28. J. D. Lin, J. G. Duh, Fracture toughness and hardness of ceria – and yttria – doped tetragonal zirconia ceramics, Materials Chemistry and Physics 78 (2002) 253 – 261

29. J. Luo, R. Stevens, Porosity-dependence of elastic moduli and hardness of 3Y-TZP ceramics, Ceramics International 25 (1999) 281 – 286
30. L. B. Garrido, E. F. Aglietti, L. Martorello, M. A. Camerucci, A. L. Cavalieri, Hardness and fracture toughness of mullite-zirconia composites obtained by slip casting, Materials Science and Engineering: A 419 (2006) 290 – 296
31. S. Heiroth, R. Ghisleni, T. Lippert, J. Michler, A. Wokaun, Optical and mechanical properties of amorphous and crystalline yttria-stabilized zirconia thin films prepared by pulsed laser deposition, Acta Materialia 59 [6] (2011) 2330 – 2340
32. R. O. Ritchie, Mechanisms of fatigue-crack propagation in ductile and brittle solids, International Journal of Fracture 100 (1999) 55– 83
33. H. Chen, Y. Zhang, C. Ding, Tribological properties of nanostructured zirconia coatings deposited by plasma spraying, Wear 253 (2002) 885 – 893
34. Y. He, L. Winnubst, A. J. Burggraaf, H. Verweij, P. G. Th. van der Varst, B. de With, Influence of porosity on friction and wear of tetragonal zirconia
35. J. H. Ouyang, S. Sasaki, Microstructure and tribological characteristics of ZrO_2 – Y_2O_3 ceramic coatings deposited by laser – assisted plasma hybrid spraying, Tribology International 35 (2002) 255 – 264
36. G. Stachowiak, Wear. Materials, mechanisms and practice, John Willey & Sons, Ltd. London, England. 2006
37. F. Vargas, H. Ageorges, P. Fournier, P. Fauchais, M. E. López, Mechanical and tribological performance of Al_2O_3-TiO_2 coatings elaborated by flame and plasma spraying, Surface & Coatings Technology 205 (2010) 1132 – 1136
38. R. S. Lima, C. Moreau, B. R. Marple, HVOF-sprayed coatings engineered from mixtures of nanostructured and submicron Al_2O_3-TiO_2 powders: An enhanced wear performance, Journal of Thermal Spray Technology, 16 (2007) 866 – 872

39. M. Wang, L. L. Shaw, Effects of the powder manufacturing method on microstructure and wear performance of plasma sprayed alumina – titania coatings, Surface & Coatings Technology 202 (2007) 34 – 44
40. T. E. Fischer, Z. Zhu, H. Kim, D. S. Shin, Genesis and role of wear debris in sliding wear of ceramics, Wear 245 (2000) 53 – 60
41. H. Schneider, S. Komarneni, Mullite, WILEY-VCH Verlag GmbH & Co. KGaA, Weinheim – GERMANY, 2005
42. E. Le Bourhis, T. Rouxel, Indentation response of glass with temperature, Journal of Non – Crystalline Solids 316 [1] (2003) 153 – 159
43. Q. Li, Y. Yu, C. S. Bhatia, L. D. Marks, S. C. Lee, Y. W. Chung, Low – temperature magnetron sputter – deposition, hardness, and electrical resistivity of amorphous and crystalline alumina thin films, Journal of Vacuum Science & Technology A18 (2000) 2333 – 2338
44. P. Nayar, A. Khanna, D. Kabiraj, S. R. Abhilash, B. D. Beake, Y. Losset, B. Chen, Structural, optical and mechanical properties of amorphous and crystalline alumina thin films, Thin Solid Films 568 (2014) 19 – 24

TABLES

Table 1. Plasma spraying parameters

Parameter	Agglomerated and sintered	Mixed and crushed
Current intensity [A]	650	
Ar-H_2 flow rate [L/min]	45 - 15	
Nozzle internal diameter [mm]	7	
Feeder type	Screw Praxair	
Powder flow rate [g/min]	16.0	22.5
Ar carrier gas pressure [bar]	5.0	
Ar carrier gas flow rate [L/min]	4.5	
Spraying distance [mm]	100 ± 1	
Sample translation speed [mm/s]	24	
Sample rotation speed [rpm]	124	
Substrate surface roughness (Ra) [µm]	8-10	
Cooling air distance [mm]	12	
Surface substrate preheating temperature [°C]	300	
Surface substrate preheating passes	18-26	
Spraying time [min]	4	
Number of spraying passes	96	92

Table 2. Wear tests parameters

Counter-body material	Alumina
Hardness of counter-body [GPa]	18.0 ± 0.5
Counter-body diameter [mm]	6
Normal load [N]	5.0
Linear speed of the sample [m/s]	0.1
Total number of cycles	20000
Radius of tests [mm]	5
Total distance of tests [m]	628
Temperature of tests [°C]	25, 500, 750 and 1000
Heating rate of tests [°C/min]*	50

* The sample and the counter-body were maintained in the furnace of tribometer at the temperature of test during 2 hours before to start each tribological essay.

Table 3. Physicochemical features of the feedstock powders

Properties		Agglomerated and sintered	Mixed and crushed
Chemical Composition (wt.%)	ZrO_2	57.52 ± 0.82	75.72 ± 0.84
	Al_2O_3	38.94 ± 0.43	19.70 ± 0.49
	Others	Balance	Balance
Phase Analysis (wt.%)	m-ZrO_2	60.4 ± 5.0	74.4 ± 4.7
	α-Al_2O_3	39.6 ± 4.3	25.6 ± 3.9
	Amorphous	----------	----------
Particle Size Distritubtion (μm)	d_{10}	15.25	29.82
	d_{50}	51.15	41.82
	d_{90}	94.12	57.12

LIST OF CAPTIONS

Figure 1. Typical residual indentation to determine: a) Fracture toughness and b) Young's modulus.

Figure 2. Typical wear track cross section to determine the wear rate.

Figure 3. Morphology of the ZrO_2-Al_2O_3 based feedstock powders: (a) Agglomerated and sintered and (b) Mixed and crushed.

Figure 4. Microstructures obtained. Bimodal ZrO_2-Al_2O_3 coating: a) Surface and b) Cross-section. Monomodal ZrO_2-Al_2O_3 coating: c) Surface and d) Cross-section. Electro-melted AZS refractory: e) Surface.

Figure 5. Porosity measured before and after the wear tests for all materials evaluated.

Figure 6. XRD patterns obtained. a) Bimodal ZrO_2-Al_2O_3 coating, b) Monomodal ZrO_2-Al_2O_3 coating and c) Electro-melted AZS refractory.

Figure 7. Crystallographic phases detected before and after the wear tests. a) Bimodal coating, b) Monomodal coating and c) Electro-melted AZS refractory.

Figure 8. Mechanical properties measured before and after the wear tests. a) Bimodal coating, b) Monomodal coating and c) Electro-melted AZS refractory

Figure 9. Wear rate of all samples evaluated.

Figure 10. Typical wear tracks obtained for the bimodal ZrO_2-Al_2O_3 coating tribologically tested at: a-c) 25 °C, d-f) 500 °C, g-i) 750 °C and j-l) 1000 °C.

Figure 11. Typical wear tracks obtained for the monomodal ZrO_2-Al_2O_3 coating tribologically tested at: a-c) 25 °C, d-f) 500 °C, g-i) 750 °C and j-l) 1000 °C.

Figure 12. Typical wear tracks obtained for the electro-melted AZS refractory tribologically tested at: a-c) 25 °C, d-f) 500 °C, g-i) 750 °C and j-l) 1000 °C.

Figure 13. Friction coefficient of all samples evaluated.

Figure 14. Wear rate of all counter-bodies evaluated.

Figure 15. Typical wear on the counter-bodies. At 25 °C: a) Bimodal, b) Monomodal, c) Refractory. At 500 °C: d) Bimodal, e) Monomodal, f) Refractory. At 750 °C: g) Bimodal, h) Monomodal, i) Refractory. At 1000 °C: j) Bimodal, k) Monomodal, l) Refractory.

FIGURES

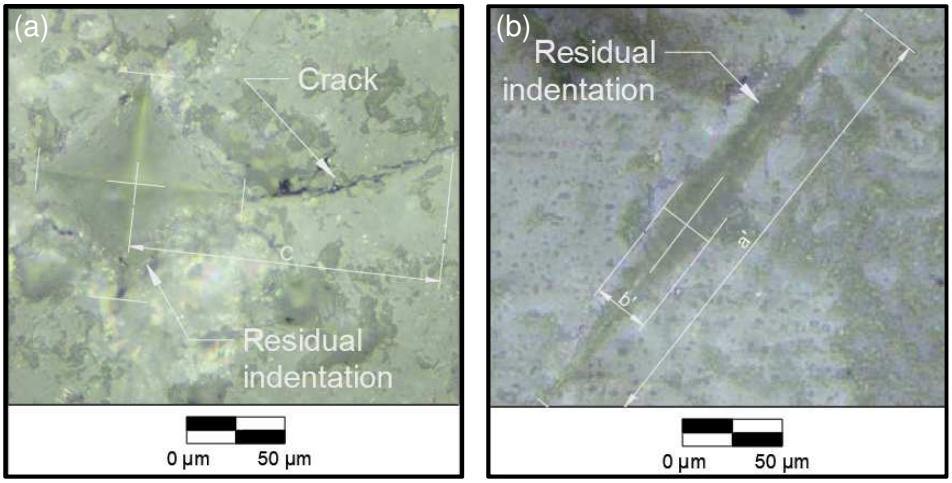

Figure 1.

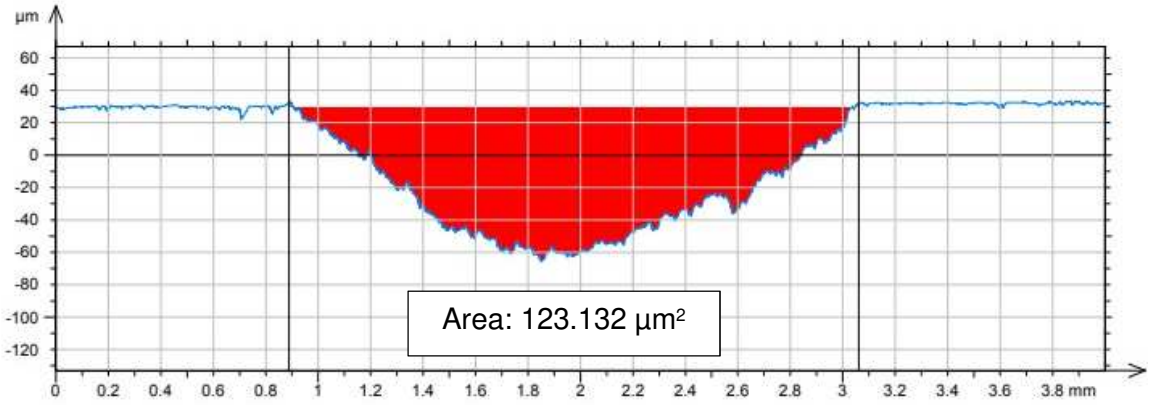
µm
60
40
20
0
-20
-40
-60
-80
-100
-120
0
0.2
0.4
0.6
0.8
1
1.2
1.4
1.6
1.8
2
2.2
2.4
2.6
2.8
3
3.2
3.4
3.6
3.8 mm
Area: 123.132 µm²

Figure 2.

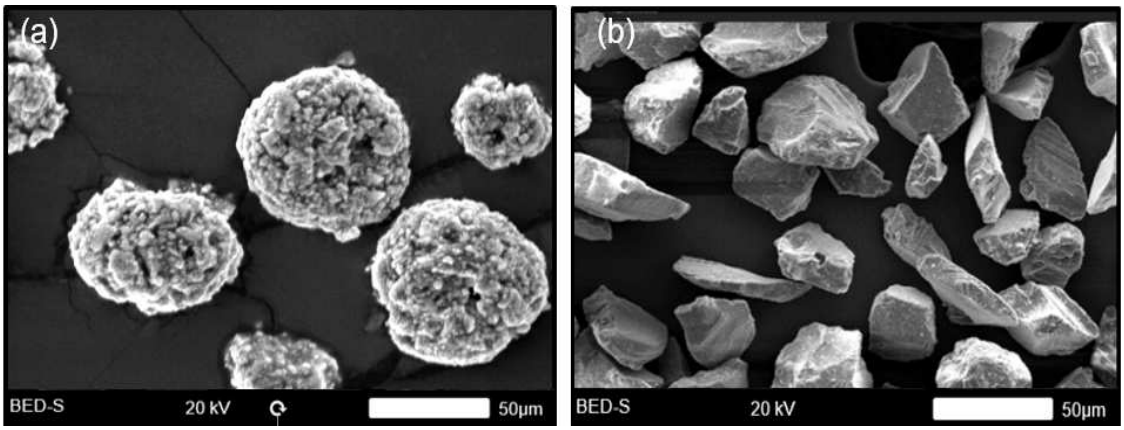

Figure 3.

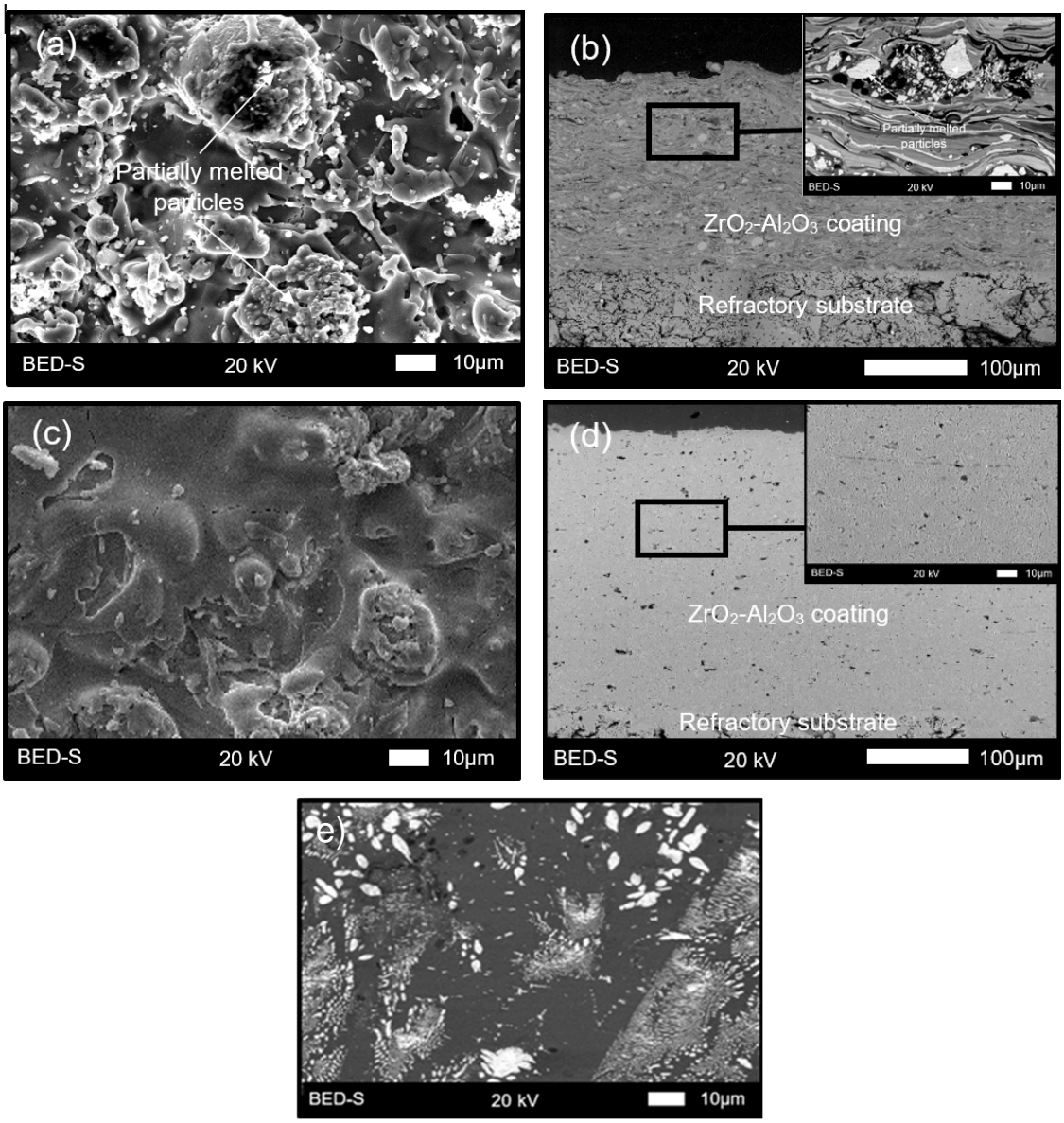
(a)
Partially melted particles
BED-S
20 kV
10μm
(b)
Partially melted particles
BED-S
20 kV
10μm
ZrO2-Al2O3 coating
Refractory substrate
BED-S
20 kV
100μm
(c)
BED-S
20 kV
10μm
(d)
BED-S
20 kV
10μm
ZrO2-Al2O3 coating
Refractory substrate
BED-S
20 kV
100μm
(e)
BED-S
20 kV
10μm

Figure 4.

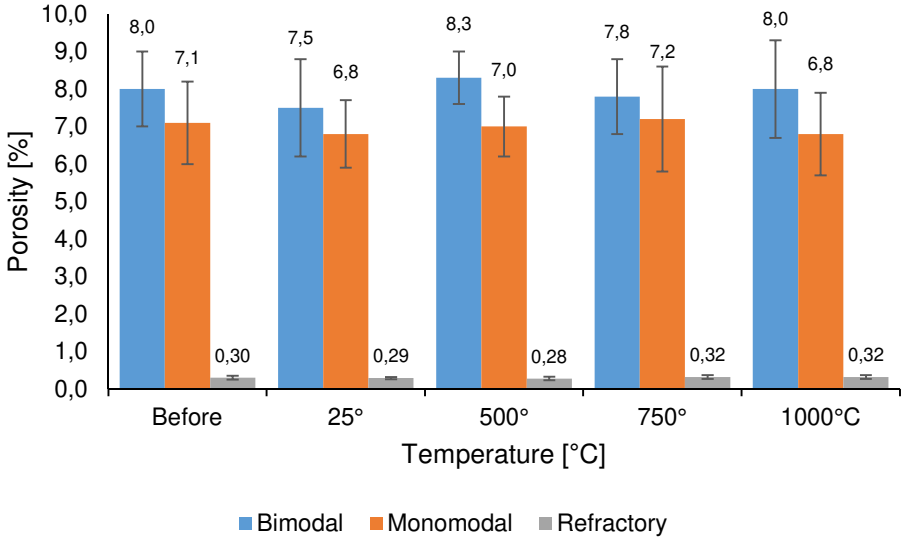
10,0
9,0
8,0
7,0
6,0
5,0
4,0
3,0
2,0
1,0
0,0
Porosity [%]
8,0
7,1
0,30
7,5
6,8
0,29
8,3
7,0
0,28
7,8
7,2
0,32
8,0
6,8
0,32
Before
25°
500°
750°
1000°C
Temperature [°C]
Bimodal
Monomodal
Refractory

Figure 5.

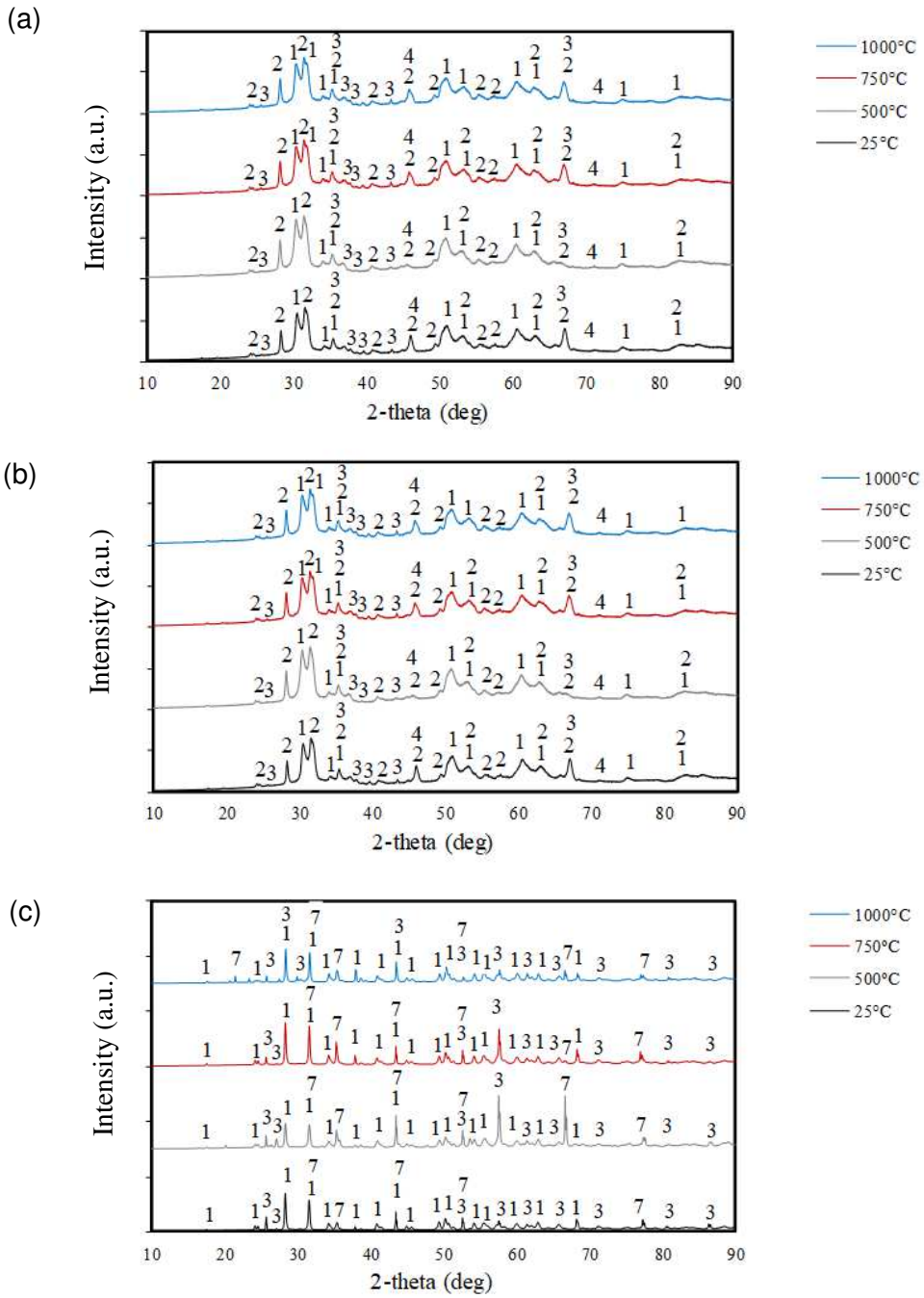

1. ZrO_2-t 2. ZrO_2-m 3. Al_2O_3-α 4- Al_2O_3-γ
5. ZrO2-c 6. YZr_8O_{14} 7. Mullite

Figure 6.

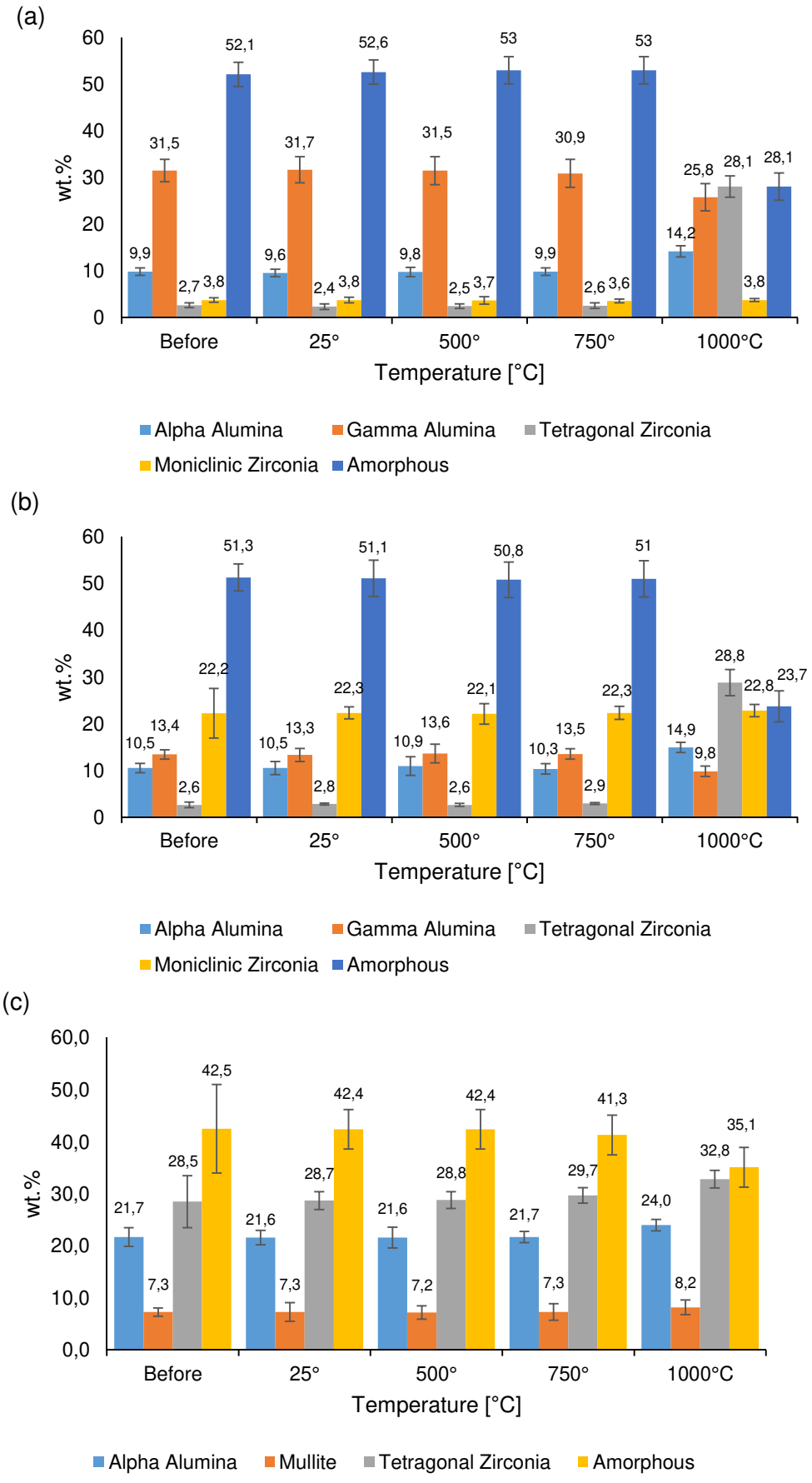
(a)
wt.%
60
50
40
30
20
10
0
9,9
31,5
2,7
3,8
52,1
9,6
31,7
2,4
3,8
52,6
9,8
31,5
2,5
3,7
53
9,9
30,9
2,6
3,6
53
14,2
25,8
28,1
3,8
28,1
Before
25°
500°
750°
1000°C
Temperature [°C]
Alpha Alumina
Gamma Alumina
Tetragonal Zirconia
Moniclinic Zirconia
Amorphous
(b)
wt.%
60
50
40
30
20
10
0
10,5
13,4
2,6
22,2
51,3
10,5
13,3
2,8
22,3
51,1
10,9
13,6
2,6
22,1
50,8
10,3
13,5
2,9
22,3
51
14,9
9,8
28,8
22,8
23,7
Before
25°
500°
750°
1000°C
Temperature [°C]
Alpha Alumina
Gamma Alumina
Tetragonal Zirconia
Moniclinic Zirconia
Amorphous
(c)
wt.%
60,0
50,0
40,0
30,0
20,0
10,0
0,0
21,7
7,3
28,5
42,5
21,6
7,3
28,7
42,4
21,6
7,2
28,8
42,4
21,7
7,3
29,7
41,3
24,0
8,2
32,8
35,1
Before
25°
500°
750°
1000°C
Temperature [°C]
Alpha Alumina
Mullite
Tetragonal Zirconia
Amorphous

Figure 7.

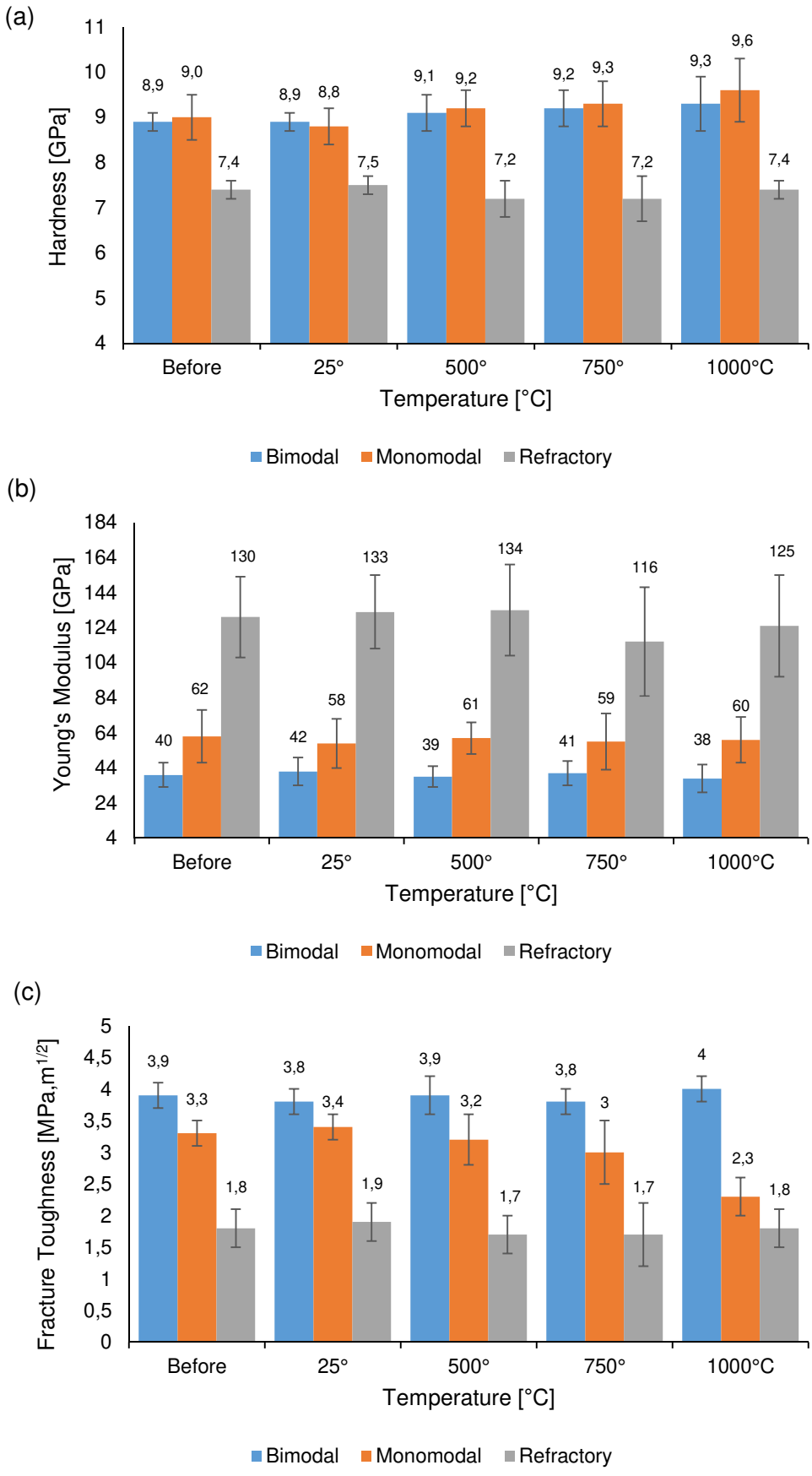
(a)
Hardness [GPa]
11
10
9
8
7
6
5
4
8,9
9,0
7,4
8,9
8,8
7,5
9,1
9,2
7,2
9,2
9,3
7,2
9,3
9,6
7,4
Before
25°
500°
750°
1000°C
Temperature [°C]
Bimodal
Monomodal
Refractory
(b)
Young's Modulus [GPa]
184
164
144
124
104
84
64
44
24
4
40
62
130
42
58
133
39
61
134
41
59
116
38
60
125
Before
25°
500°
750°
1000°C
Temperature [°C]
Bimodal
Monomodal
Refractory
(c)
Fracture Toughness [MPa,m1/2]
5
4,5
4
3,5
3
2,5
2
1,5
1
0,5
0
3,9
3,3
1,8
3,8
3,4
1,9
3,9
3,2
1,7
3,8
3
1,7
4
2,3
1,8
Before
25°
500°
750°
1000°C
Temperature [°C]
Bimodal
Monomodal
Refractory

Figure 8.

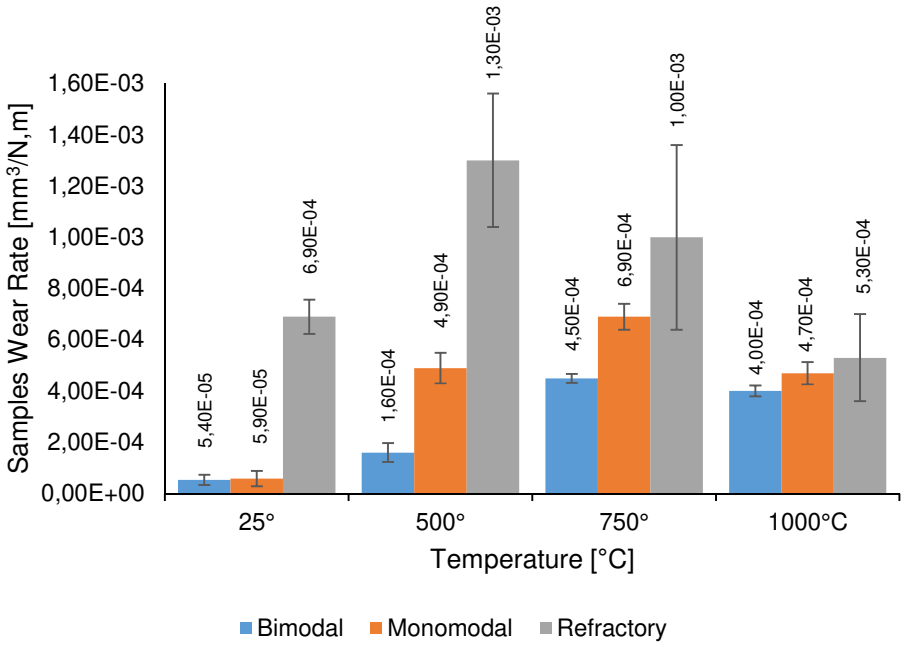
Samples Wear Rate [mm3/N,m]
1,60E-03
1,40E-03
1,20E-03
1,00E-03
8,00E-04
6,00E-04
4,00E-04
2,00E-04
0,00E+00
5,40E-05
5,90E-05
6,90E-04
1,60E-04
4,90E-04
1,30E-03
4,50E-04
6,90E-04
1,00E-03
4,00E-04
4,70E-04
5,30E-04
25°
500°
750°
1000°C
Temperature [°C]
Bimodal
Monomodal
Refractory

Figure 9.

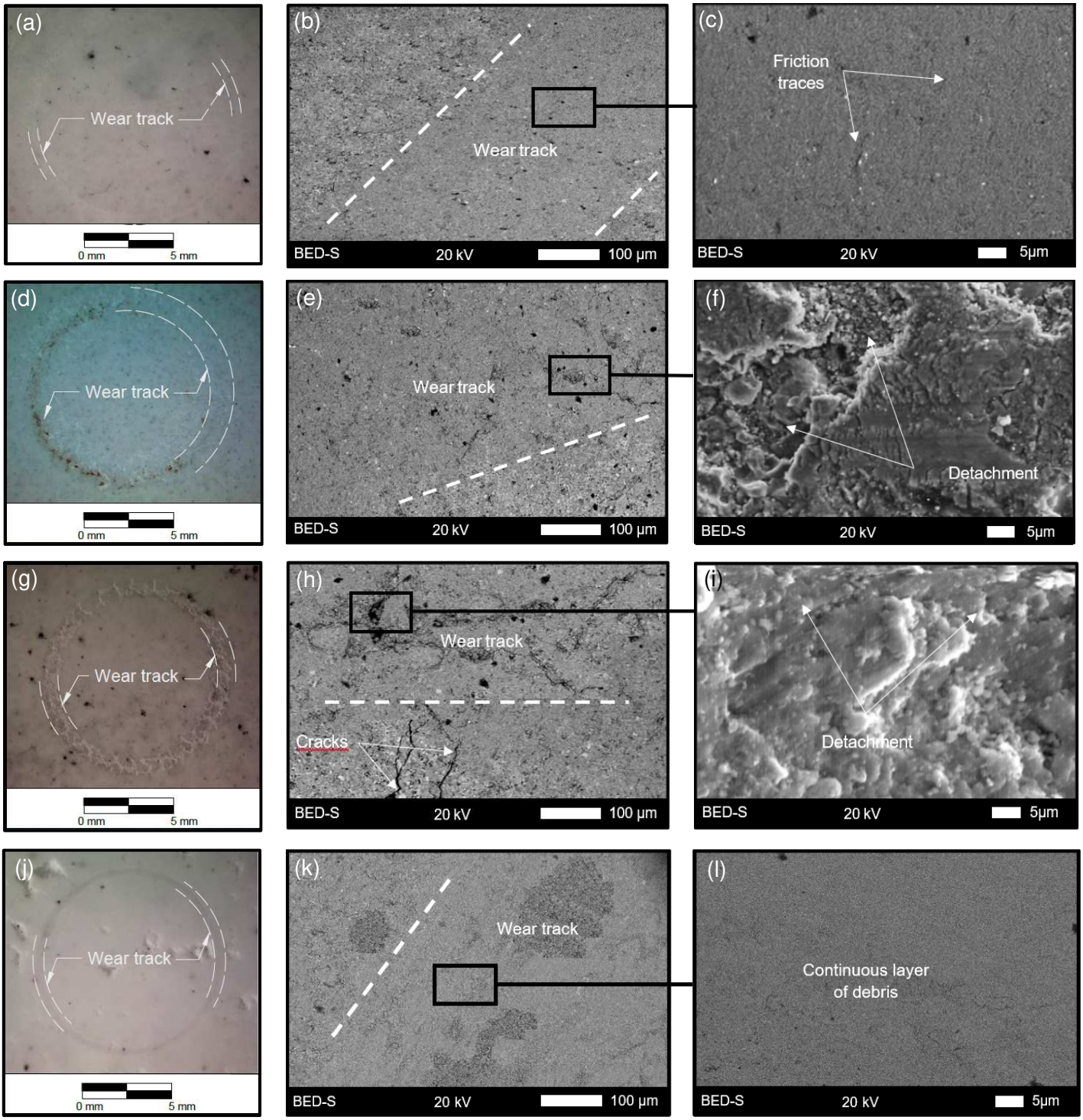
(a)
Wear track
0 mm
5 mm
(b)
Wear track
BED-S
20 kV
100 µm
(c)
Friction traces
BED-S
20 kV
5µm
(d)
Wear track
0 mm
5 mm
(e)
Wear track
BED-S
20 kV
100 µm
(f)
Detachment
BED-S
20 kV
5µm
(g)
Wear track
0 mm
5 mm
(h)
Wear track
Cracks
BED-S
20 kV
100 µm
(i)
Detachment
BED-S
20 kV
5µm
(j)
Wear track
0 mm
5 mm
(k)
Wear track
BED-S
20 kV
100 µm
(l)
Continuous layer of debris
BED-S
20 kV
5µm

Figure 10.

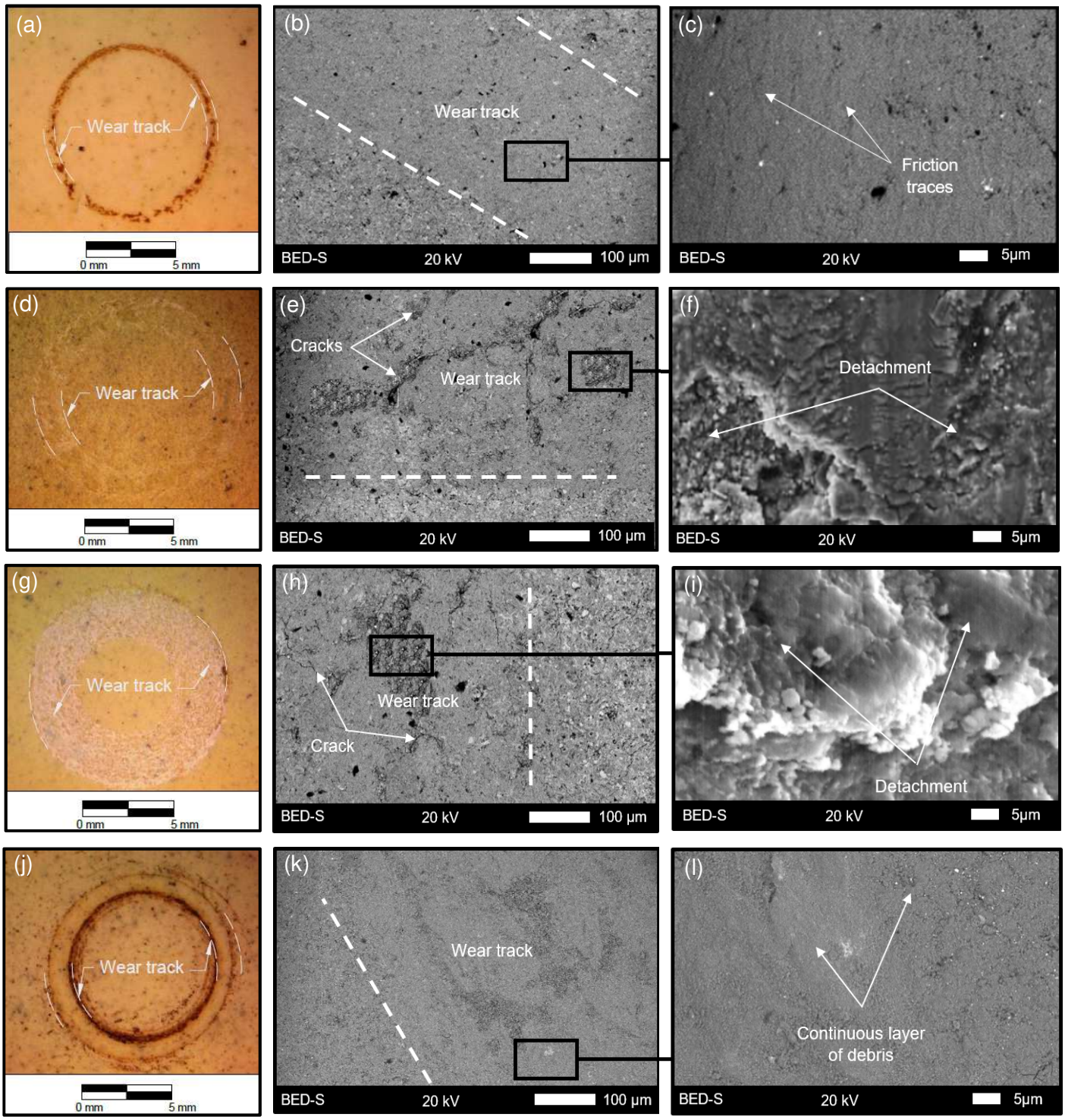
(a)
Wear track
0 mm
5 mm
(b)
Wear track
BED-S
20 kV
100 µm
(c)
Friction traces
BED-S
20 kV
5µm
(d)
Wear track
0 mm
5 mm
(e)
Cracks
Wear track
BED-S
20 kV
100 µm
(f)
Detachment
BED-S
20 kV
5µm
(g)
Wear track
0 mm
5 mm
(h)
Wear track
Crack
BED-S
20 kV
100 µm
(i)
Detachment
BED-S
20 kV
5µm
(j)
Wear track
0 mm
5 mm
(k)
Wear track
BED-S
20 kV
100 µm
(l)
Continuous layer of debris
BED-S
20 kV
5µm

Figure 11.

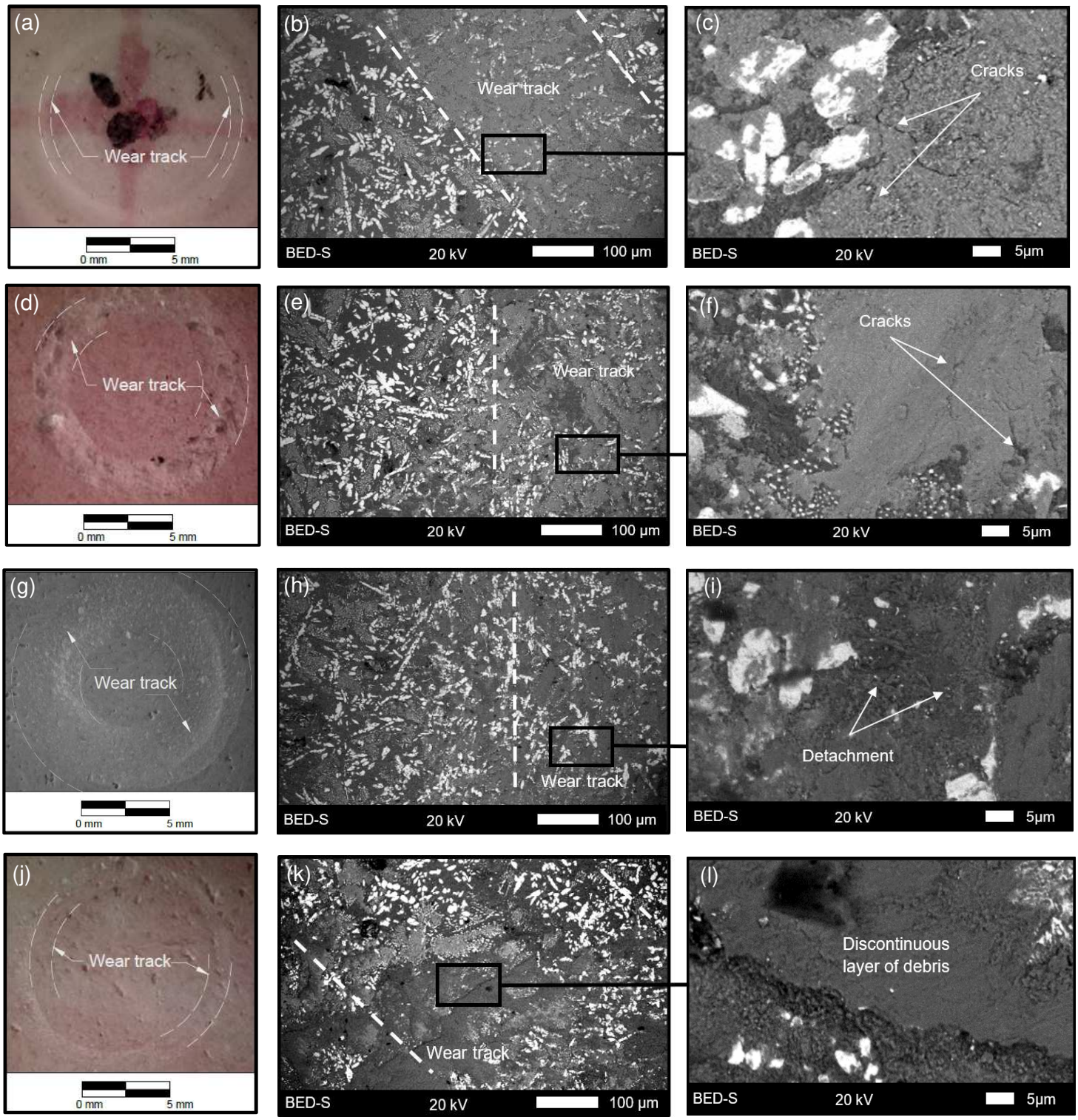
(a)
Wear track
0 mm
5 mm
(b)
Wear track
BED-S
20 kV
100 µm
(c)
Cracks
BED-S
20 kV
5µm
(d)
Wear track
0 mm
5 mm
(e)
Wear track
BED-S
20 kV
100 µm
(f)
Cracks
BED-S
20 kV
5µm
(g)
Wear track
0 mm
5 mm
(h)
Wear track
BED-S
20 kV
100 µm
(i)
Detachment
BED-S
20 kV
5µm
(j)
Wear track
0 mm
5 mm
(k)
Wear track
BED-S
20 kV
100 µm
(l)
Discontinuous
layer of debris
BED-S
20 kV
5µm

Figure 12.

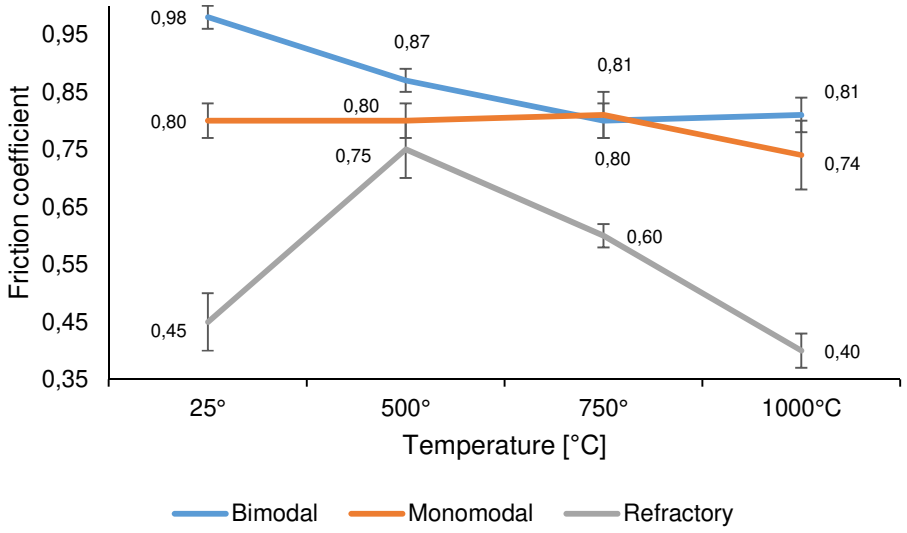
Friction coefficient
0,95
0,85
0,75
0,65
0,55
0,45
0,35
0,98
0,87
0,81
0,81
0,80
0,80
0,74
0,75
0,80
0,60
0,45
0,40
25°
500°
750°
1000°C
Temperature [°C]
Bimodal
Monomodal
Refractory

Figure 13.

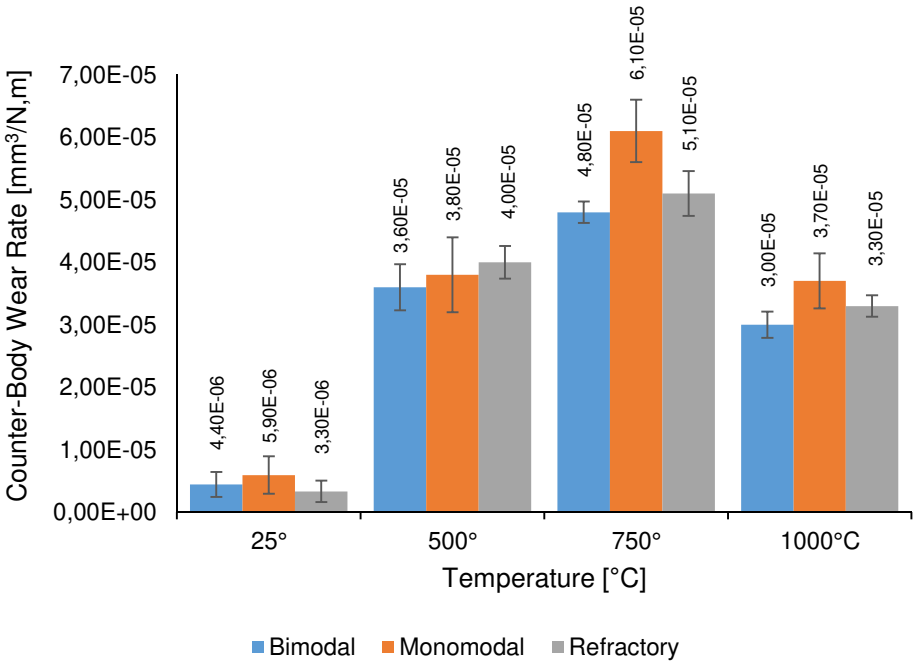
Counter-Body Wear Rate [mm³/N,m]
7,00E-05
6,00E-05
5,00E-05
4,00E-05
3,00E-05
2,00E-05
1,00E-05
0,00E+00
4,40E-06
5,90E-06
3,30E-06
3,60E-05
3,80E-05
4,00E-05
4,80E-05
6,10E-05
5,10E-05
3,00E-05
3,70E-05
3,30E-05
25°
500°
750°
1000°C
Temperature [°C]
Bimodal
Monomodal
Refractory

Figure 14.

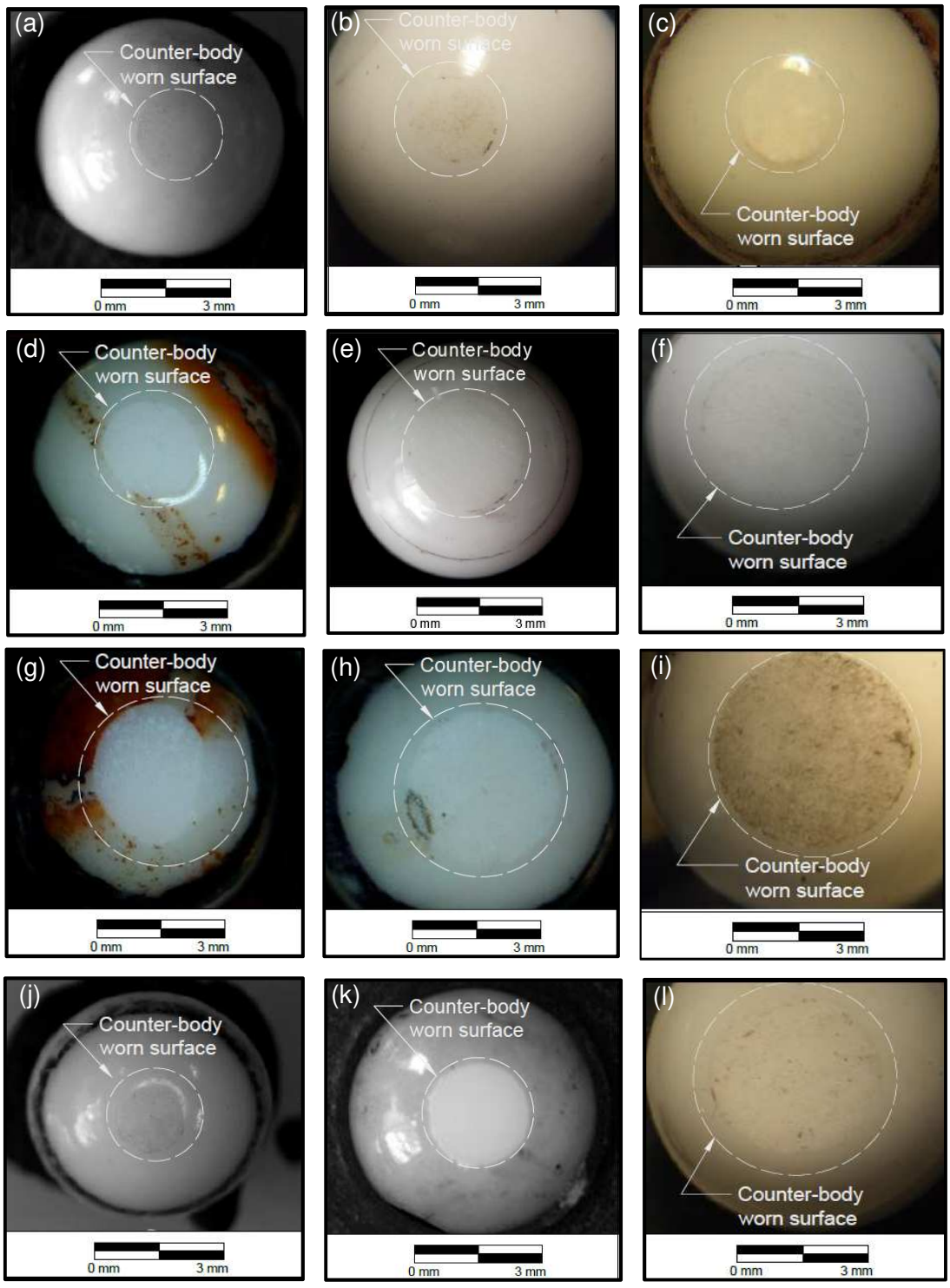
(a)
Counter-body worn surface
0 mm
3 mm
(b)
Counter-body worn surface
0 mm
3 mm
(c)
Counter-body worn surface
0 mm
3 mm
(d)
Counter-body worn surface
0 mm
3 mm
(e)
Counter-body worn surface
0 mm
3 mm
(f)
Counter-body worn surface
0 mm
3 mm
(g)
Counter-body worn surface
0 mm
3 mm
(h)
Counter-body worn surface
0 mm
3 mm
(i)
Counter-body worn surface
0 mm
3 mm
(j)
Counter-body worn surface
0 mm
3 mm
(k)
Counter-body worn surface
0 mm
3 mm
(l)
Counter-body worn surface
0 mm
3 mm

Figure 15.